Journal Pre-proof

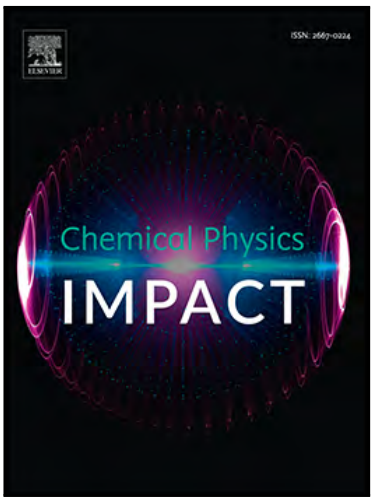

Rare earth Gd^{3+}-substituted Co spinel nanoferrites structural, dielectric and magnetic properties

K. Vani , N. Hari Kumar , D. Ravinder , G. Naveena , B. Sathish , G. Sriramulu

PII: S2667-0224(24)00129-4
DOI: https://doi.org/10.1016/j.chphi.2024.100585
Reference: CHPHI 100585

To appear in: *Chemical Physics Impact*

Received date: 19 November 2023
Revised date: 22 March 2024
Accepted date: 25 March 2024

Please cite this article as: K. Vani , N. Hari Kumar , D. Ravinder , G. Naveena , B. Sathish , G. Sriramulu , Rare earth Gd^{3+}-substituted Co spinel nanoferrites structural, dielectric and magnetic properties, *Chemical Physics Impact* (2024), doi: https://doi.org/10.1016/j.chphi.2024.100585

Rare earth Gd^{3+}-substituted Co spinel nanoferrites structural, dielectric and magnetic properties

K. Vani[1], N. Hari kumar[2], D. Ravinder[1]*, G. Naveena[1], B. Sathish[1], G. Sriramulu[1]

[1]*Department of Physics, Osmania University, Telangana, 500007, Hyderabad, India*

[2]*Department of Physics, St.Mary 's Group of Institutions, Deshmukhi, Yadadri Bhongiri 508116,India*

*Corresponding author: aknhkou@gmail.com, ravindergupta29@rediffmail.com

Abstract

Gadolinium-doped cobalt ferrite $CoGd_xFe_{2-x}O_4$ (CGF) were produced using citrate gel auto-combustion method (x = 0-0.025 at an interval of 0.005). An investigations on the impact of Gd^{3+} ions on structural, dielectric, and magnetic properties were conducted. The synthesized materials were characterized using the following techniques: X-ray diffraction (XRD), scanning electron microscopy (SEM), Fourier transform infrared (FTIR) spectroscopy, ultraviolet visible spectroscopy (UV), impedance (dielectric) analysis, and vibrating sample magnetometer (VSM). The crystalline size ranging from 48 to 13 nm. The Williamson-Hall plots were utilized to examine the impact of crystalline size and lattice strain on the peak broadening of each sample. The X-ray diffraction spectra were used to confirm phase identification and spinel structure. The results of FTIR examinations show that strong metal oxide bonds can be found in the tetrahedral and octahedral sites at wavelengths of 351–376 cm^{-1} and 567–574 cm^{-1}, respectively. The obtained samples to study optical energy bandgap (Eg), which vary from 2.01 eV to 2.45 eV and show that they are semiconducting materials.The Maxwell-Wagner model and Koop's theory have both been used to study the behaviour of dielectric properties. The dielectric constant at room temperature to 673 K in the frequency range 50 Hz–1 MHz to study the dielectric constant, dielectric loss, AC electrical conductivity, and impedance. The impedance charts show how conductivity was impacted by grain and grain boundary mechanisms. In relation to an applied field of 100 kOe, magnetization was measured at 3K and 300K. The blocking temperature (T_B), which exhibits super-paramagnetic behaviour, is found to be approximately 359K according to zero-field cooling ZFC and field cooling. The FC experiments carried out in the temperature range of 3K–360K under an applied field of 100 Oe.

Keywords: Spine ferrites; Dielectric studies; Low temperature magnetization; Applications.

1. Introduction

The spinel ferrites are particularly important magnetic materials because of their distinctive combination of electric and magnetic characteristics. The advantageous for a variety of technological uses, such as high-density magnetic recording, microwave devices, electric insulators, memory cores, high-frequency applications, as a catalytic treatment for human illness, magnetic bioseparation, drug delivery, sensors, magnetic resonance imaging, and hypothermia. The depending on the application, the fundamental electrical and magnetic properties can be changed [1]. The spine ferrites have the chemical formula MFe_2O_4 (where M is Ni, Co, Zn, etc.), in which Fe occupies the octahedral (B) site and M occupies the tetrahedral (A) site, and oxygen anions form a face-centred cubic structure that is tightly packed [2, 3]. The unique electrical, optical, and magnetic properties of cobalt-based spinel ferrites ($CoFe_2O_4$), which crystallise in inverse spinel structure in bulk materials. The spinel cubic structure space group Fd-3m in nanoparticles, and are of great interest [4–5]. These properties include a high Curie temperature, moderate saturation magnetization, large magnetocrystalline anisotropy, a large magnetostrictive coefficient, excellent chemical stability, and good thermal stability. The synthesis method can significantly affect the physical and chemical characteristics of cobalt ferrites by substituting different cations at tetrahedral or octahedral locations [6]. As a result, the rare earth lanthanides are commonly used to adjust the properties of cobalt ferrites in order to improve their remarkable qualities because they are very good electrical insulators with high resistance [7]. M. Hasim et al. conducted research on the substitution of RE = Ce, Dy on cobalt ferrites, which demonstrated that increasing the Ce and Dy concentrations increases coercivity while decreasing magnetization values [8]. C. Murugesan et al. substituted Gd on cobalt ferrites and found that the dielectric constant increases as Gd concentration increases [9]. Aravind Kumar et al. synthesised Gd-substituted cobalt ferrites and discovered that the dielectric constant decreases as Gd concentration and frequency increase [10]. Erum Pervaiz et al. prepared Gd-doped cobalt ferrites and reported that room-temperature DC electric resistivity increases to $9.5x10^7$ with Gd concentration except for x=0.025 (~10^6) and that dielectric constant and dielectric loss decrease to 4.9 and 0.016, respectively, with increased dopant concentration and soft magnetic behaviour due to Gd substitution [11]. M. Kamran et al. developed La-doped cobalt ferrites and observed that increasing La doping reduces dielectric constants, dielectric losses, and AC conductivity values,

while increasing La concentration increases DC electric resistivity [12]. L. Avazpour developed Eu and Nd-doped cobalt ferrites and discovered that at room temperature, the saturation magnetization of the ferrite ceramics decreases with grain size [13].

The single-phase development of the cubic spinel structure is confirmed by the fourier transform infrared and Raman spectra.The magnatic and dielectric properties of Gd^{3+} substitution Co ferrites were studied by Kadam [14]. A cubic spinel phase forms without the existence of an ambiguity peak, according to the examination of x-ray diffractograms (XRD). The transmission electron microscopy image revealed spherical particles with a mean diameter of 27 nm. By using the ferrite's SAED picture, the peaks identified by the XRD data were confirmed. The magnetic characteristics, such as coercivity, retentivity, and saturation magnetization, were measured using the VSM data [15]. The creation of single-phase spinel with a high degree of crystallinity was discovered using an X-ray diffractometer (XRD). Both the production of spinel matrix crystallographic sites and the formation of agglomerated spherical particles with nanometric sizes were confirmed by Fourier transform infrared (FTIR) and transmission electron microscopy (TEM) experiments. A week of ferrimagnetic behaviour is shown at low temperatures, whereas a super-paramagnetic behaviour is seen at high temperatures, according to the analysis of magnetic characteristics [16].

The cobalt ferrite were suggested to have a small number of gadolinium ions substituted in order to enhance their structural, dielectric, and magnetic characteristics. The citrate gel auto-combustion method is used to explore the low-temperature magnetic (x = 0.020) and dielectric properties of CGF (x = 0-0.025 in a range of 0.005) ferrites.

2. Experimental details

2.1 sample preparation

The chemical formula CGF with X = 0, 0.005, 0.010, 0.015, 0.020, and 0.025 was used to make gadolinium-substituted cobalt ferrites. The chemical Cobalt, ferric, gadolinium, and citric nitrates are used as reactants in the first stage. Weighing the necessary quantity of reactants reveals that the molar ratio of metal nitrate to citric acid is 1:3. To make a homogeneous solution, citric acid and weighted metal nitrates are dissolved in deionized water and swirled together with a magnetic stirrer. By continuously swirling while adding 25% ammonia solution, the solution's pH is brought down to 7, as desired. The resulting nitrate-citrate solution is heated on a hot plate of a magnetic stirrer to about 373 K

until it forms a highly viscous and dry gel, then allowed to condense. The dried gel is then heated on a hot plate to 473 K` until auto-combustion occurs as a result of self-ignition. CGF nanopowder is the final product. The nanopowder was ground into a fine powder. The powder was then heated to create pellets. The pellets were then sintered and characterised using various techniques. The synthesis flow chart is shown in Fig. 1.

3. Results and discussion

3.1 XRD analysis

The X-ray diffraction patterns of CGF (x = 0-0.025 in an interval of 0.005) ferrites are shown in Figure 2, with a distinct Bragg's reflection seen for the strongest peak without any impurity phases. The diffraction peaks planes observe at (220), (311), (400), (422), (511), (440), and (533) for the most strong peaks at 30.1°, 35.5°, 43.1°, 53.5°, 57.0°, 62.6°, 74.1° and with JCPDS Card No. 22-1086. This study demonstrated the production of cobalt nanoferrites cubic spinel structure with the Fd3m space group [17, 15]

The structural parameters such as lattice constant (a), unit cell volume (V), crystallite size (D), and X-ray density (dx) were computed using the following formulas (1-5) and are presented in Table 1.

$a = d\sqrt{h^2 + k^2 + l^2}$ ------ (1),

where d is the inter-planar spacing, (h k l) are the miller indices.

$V = a^3$------ (2)

here 'a' is lattice constant,

$D = \frac{K\lambda}{\beta cos\theta}$ ------ (3)

Debye-Scherer's formula, where K is a dimensionless shape factor having a value between 0.9 and 1, is a diffractometer with an X-ray wavelength (CuK_α source i.e. λ= 1.5406 Å), β is the line broadening at full width at half-maximum of each phase (in radians), and θ is the Bragg angle (in degrees), is used to calculate these quantities.

$dx = \frac{8M}{VN}$ ------ (4),

where M is the molecular weight of the sample, V is the volume of the unit cell, N is Avogadro's number (6.023×10^{23}).

For ferrites, the hopping lengths L, i.e. the distance between the magnetic ions, effects the physical properties, reported by various authors. The hopping length foe site A and B are represented by L_A and L_B were calculated by using the equations

$L_A = \frac{a\sqrt{3}}{4}$ Å and $L_B = \frac{a\sqrt{2}}{4}$ Å ------ (5),

where a is the lattice parameter.

When Gd is incorporated into cobalt ferrite, the lattice constant (a) value increases due to the difference in the ionic radii of Gd^{3+} (1.107), which is bigger than the ionic radii of Fe^{3+} (0.76) [18]. The crystallite sizes were determined to be 48.27, 34.64, 31.07, 24.01, 22.91, and 13.01 nm (x= 0, 0.005, 0.010, 0.015, 0.020, 0.025) and decreased with increasing Gd concentration. Actual broadening of diffraction peaks corrected for experimental (β_{ex}) and instrumental widening (β_{in}) as $\beta = \beta_{ex}^2 - \beta_{in}^2$. Taking into account the size and strain effects, the Williamson-Hall equation for actual broadening (β) can be modelled as follows:

$\beta = \frac{K\lambda}{Dcos\theta} + 4\varepsilon tan\theta$ ----- (6)

where $\left(\frac{K\lambda}{\boldsymbol{Dcos\theta}}\right)$ **is** broadening due to the size (D) and 4$\boldsymbol{\varepsilon}$tan$\boldsymbol{\theta}$ is broadening due to strain ($\boldsymbol{\varepsilon}$)[19-20]. After modification of above equation yields,

i.e., $\beta cos\theta = \frac{0.9\lambda}{D} + 4\varepsilon sin\theta$ ----- (7)

Figure 3 depicts the W-H plots of the prepared samples, whereas Figure 4 depicts the change in crystalline size and micro strain with regard to composition.

3.2 FTIR analysis

FTIR was used to study the metal ion stretching and functional groups of the gadolinium-doped cobalt ferrite nanoferrites. The synthesised CGFferrites FTIR spectra are displayed in Figure 5 in the 400-4000 cm^{-1} range. The infrared spectra of ferrites with the formula MFe_2O_4, where M is a divalent metal, consist of two absorption bands that result from the stretching of bonds between tetrahedral or octahedral metal ions and oxide ions. The specifically the band ranges ν_1 (540-600 cm^{-1}) and ν_2 (330-400 cm^{-1}) [21-22]. While the other band in the range ν_2 (380-350 cm^{-1}) is attributed to the stretching of metal at the octahedral site, the band with the larger wave number found in the range ν_1 (580-560 cm^{-1}) relates to the vibrations of the metal at the tetrahedral site reported in Table 2. The creation of the spinel ferrite structure in the produced nanoferrites is

confirmed by the presence of these absorption bands. Additionally, when cobalt ferrite is doped with gadolinium, the lattice induces strain, which causes Fe^{3+} ions to move from tetrahedral positions to octahedral sites. This results in an increase in ionic radii and a modification of the bond length (Fe-O) at both locations, which results in the shift towards high frequency seen in figure 5.

The force constant of ions at tetrahedral and octahedral sites can be calculated using the relation.

$$k = 4\pi^2 c^2 \nu^2 \mu \text{ ----- (8)}$$

Where k is the force constant, c is the speed of light ($3x10^8$ m/s), v is the vibration frequency of the tetrahedral (ν_1) and octahedral (ν_2) sites, and is the decreased mass for the Fe^{3+} and O^{2-} ions (-$2.065X10^{-26}$ kg/mol). Table 2 lists the values of the calculated force constants, k_T and k_O.

At the tetrahedral and octahedral locations of the prepared gadolinium doped cobalt nanoferrites, the variation in force constant suggests variation in the bond length of cations and oxygen ions. Figure 6 depicts the fluctuation of force constants with composition. The absorption bands in the 1530 cm^{-1} to 1545 cm^{-1} range are due to nitrate (NO^{3-}) ion vibrations, the bands in the 2315 cm^{-1} to 2890 cm^{-1} range are credited to carbon groups, and the bands in the 3410 cm^{-1} to 3525 cm^{-1} range are attributed to OH-groups. Gadolinium doping results in considerable alterations to the structural characteristics.

3.3 UV- Visible spectroscopy analysis

UV-Visible spectroscopy was employed to determine the bandgap energy and confirm the semiconductor nature. The UV-Visible absorption spectra of CGF (x= 0-0.025 in an interval of 0.005) nanoferrite samples at room temperature are shown in Figure 7 in the 200-800 nm range. It has been found that the electron evolution between oxygen ions and cations is what causes the variation in the absorption slope. Tauc Equation was used to get the bandgap energy (Eg).

$$\alpha h\nu^{\gamma} = A(h\boldsymbol{\nu} - \boldsymbol{E_g}) \text{ ----- (9)}$$

Where α is the absorption coefficient, h is Planck's constant, ν is the frequency of the incident photon, A is proportionality constant and γ denotes the nature of the electronic transition i.e., when γ=2 and γ=1/2 represents direct and indirect allowed transition respectively.

From the literature survey it has been observed that the ferrites like $CoFe_2O_4$, $NiFe_2O_4$ and $ZnFe_2O_4$ exhibit only a direct bandgap [23-24]. The Tauc plots of $(\alpha\alpha h\nu)^2$ against hν for all the samples are shown in figure 8. The extrapolation of the linear regions of the plots (i.e.$(\alpha h\nu)^2 = 0$) onto the x-axis gives the direct bandgap or edge values. The bandgap energy values for the prepared samples are found to be 2.45eV, 2.35eV, 2.30eV, 2.23eV, 2.10eV and 2.01eV respectively. It is observed that by increasing the concentration of Gd bandgap decreases. Because the obtained values fell inside the semiconducting range, the optical bandgap (Eg) of the produced samples demonstrated their semiconducting nature. The energy bandgap values of the gadolinium doped cobalt ferrites samples reported by Y.Lu et al.[25] were 2.04 eV - 2.28 eV, respectively, and are comparable to those in our investigation.

According to the findings, the absorption band moved a little bit into the visible range when the cerium level rose. The absence of shoulders and extremely sharp edges in the absorption bands of Gd-Co ferrites suggests that an intrinsic band transition, rather than surface states, may be the cause of absorption in the visible light spectrum. Gd^{2+}, Co^{2+}, and Fe^{3+} cations occupy the tetrahedral and octahedral sites in the standard spinel-type compound Gd-Co ferrite, respectively. The valence band of the Gd-Co ferrite band structure is typically identified as the Fe-3d orbital, while the conduction band is the O-2p orbital. The electron excitation from the O-2p level into the Fe-3d level is responsible for the visible light absorption spectra of Co-Zn ferrite.Because of the larger particles, there is an increase in the band gap energy (Eg) and a shift in the bands to higher wavenumbers with increasing Gd^{3+} concentration [20]. It has been found that composition affects where absorption bands are located.

3.4 Dielectric studies

The dielectric investigations shed light on the material's method of electric conduction. In order to study the dielectric properties of gadolinium-doped cobalt ferrites, a bode 100 impedance analyzer with a frequency range of 50Hz to 5MHz is used at room temperature as well as between 307 K and 773 K. Utilising the formula [26], the values of the dielectric constant with applied frequency are determined.

$$\varepsilon\varepsilon' = \frac{ccd}{\varepsilon\varepsilon_o AA} \text{ ----- (10)}$$

Where A is the cross-sectional area of the pellet, d is its thickness, ε_o is its permittivity, and C is its capacitance.

3.5 Variation of DC electrical resistivity

The ferrites electric properties are greatly impacted by the synthesis process, the kind and substitution of doped cations at the A and B sites. The particle's size and shape depends upon, and the sintering temperature. For the CGF (x = 0-0.025 in an interval of 0.005) ferrite at 300K to 700K, a two probe technique was utilised to investigate the dependence of DC electric resistivity. Figure 9. demonstrates how, at normal temperature, composition affects DC electrical resistivity [27–30]. The figure shows that the DC electrical resistivity decreases with a rise in gadolinium concentration at room temperature, with the exception of 0.020. This decrease in resistivity can be the result of Fe^{3+} ions replacing other ions at the A-site, which increases the concentration of Fe^{3+} ions at the B-site.

3.6 Impedance Analysis

The electrical behaviour of materials is examined via impedance analysis. Information on the grain and grain boundary contributions to microstructure resistances is provided by the impedance analysis. Additionally, it gives full details regarding the facts on how resistive (actual part) Z and reactive (imaginary part) Z′ components contribute to conductivity when an alternating field is applied. At room temperature and between 307 K and 673 K for CGF (x = 0-0.025 in an interval of 0.005), impedance analysis has been done in the frequency range of 50Hz to 5MHz. Figures 10(a-f) and 11(a-f) show how the real and imaginary parts of the impedance have been shown as functions of frequency at various chosen temperatures [31-33]. The figure shows that both Z′ and Z″ have higher magnitudes at low frequencies, which diminish as frequency increases, and that at higher frequencies, both Z′ and Z″ become constant for all compositions. Additionally, all samples experience a drop in Z′ and Z″ magnitude as the temperature rises. The observed Z′ and Z″ behaviour for all samples in the low- and high-frequency areas is consistent with the findings for spinel ferrites reported in the literature [34-36]. Figures 11 (a-f) further show that at a given temperature, there is only one peak at a given frequency (the relaxation frequency), and that as the temperature rises, the relaxation frequency changes upward and the peak height declines.

Complex impedance was plotted between real portion of impedance (Z′) and imaginary part of impedance (Z″), or Nyquist plot, in order to analyse the contribution of grains and grain boundaries in conduction mechanism. Figures 12 and 13 (a-f) depict the complex impedance spectra of CGF (x= 0-0.025 in an interval of 0.005) ferrite samples that were tested at room temperature and at a chosen temperature.

The plot is made up of an array of overlapping, depressed semicircles, where the diameter of the arcs stands for the resistance of the grain and grain boundary. At low frequencies, a semicircle symbolises the grain boundary, whereas at higher frequencies, it symbolizes the conduction of the grain interior. The diameter of the semicircle shrinks as temperature rises, indicating that the samples' grain resistance has decreased. Additionally, the conduction process is thermally activated, confirming the prepared samples' semiconductor nature over the entire temperature range of 623 K to 4273 K. Detectors, imaging devices, energy conversion, non-linear optics, solar cells, photocatalysis, water treatment, biomedicine, nanophotonics, nanoelectronics, and miniaturised sensors are a few of these.

3.7 Low temperature magnetic studies

The material's magnetic characteristics were investigated using the VSM. By applying a magnetic field up to around 100 kOe at 300K and 3K, measurements of the magnetic hysteresis loop of the CGF (x = 0.020) sample are made. Figure 14 (a,b) illustrates hysteresis loops. The sample exhibits ferromagnetic behaviour, as can be seen in the image. The values of the anisotropy constant (K), the saturation magnetization (Ms), the coercivity (Hc), the remanance magnetization (Mr), the remanance ratio (Mr/Ms), and the magnetic moment (BM) at 3K and 300K are provided in Table 3. It has been noted that the saturation magnetization is higher at low temperatures (3K) than it is at 300K. The decrease in thermal fluctuations and surface spin order at the particle's surface is attributed to the increase in saturation magnetization as compared to 300 K. According to the table, Hc and Mr values are very low at 300 K and will be close to zero at temperatures above room temperature. As a result, the superparamagnetic behaviour of the magnetic particles is characterised by zero coercivity and zero remanence [37].

The magnetic characteristics of the substance were examined using the VSM. By applying a magnetic field up to around 100 kOe at 300K and 3K, the magnetic hysteresis loop measurements of the CGF (x = 0.020) sample are done. Figure 14(a,b) depicts hysteresis loops. The sample exhibits ferromagnetic behaviour, which is evident from the figure. As shown in Table (3), the Ms, Hc, Mr, Mr/Ms, K, and BM values at 3K and 300K are all reported. We can see that the saturation magnetization is higher at low temperatures (3K) than it is at higher temperatures (300K).

Figure 15. displays the fluctuation of the magnetization with temperature curve for the CGF (x = 0.020) sample as measured in FC and ZFC modes in a 100 oe external magnetic field. In ZFC mode,

the sample was cooled from 360K to 3K while no magnetic field was present. Next, a measuring field of 100 ohms was added, and magnetic measurements were taken during the warming cycle. As opposed to FC mode, which involved cooling the sample from 360 K to 3 K while a measuring field was present, this mode involved monitoring the magnetization as a function of rising temperature [38].

Figure 15 shows that both ZFC and FC magnetization decrease as temperature rises. Due to the magnetic relaxation properties of the particles, FC and ZFC modes bifurcate at 359 K (the blocking temperature Tb), which supports the superparamagnetic nature of the particles. It is evident from a comparison of the hysteresis curves and FC-ZFC data that below the Tb, or less than 359K, a material exhibits some hysteresis and acts as a ferromagnetic material, and above the Tb, or more than 359K, a material behaves as a superparamagnetic material [39].

4. Conclusions

The samples of cobalt ferrites doped with gadolinium were investigated. The Williamson-Hall plot was used to examine the impact of crystalline size and lattice strain on the peak broadening of each sample, with crystalline sizes ranging from 13 to 48 nm. X-ray diffraction spectra were utilised to establish phase identification and spinel structure. The FTIR measurements show the presence of absorption bands at 380-350 cm^{-1} and 580-560 cm^{-1} that are consistent with strong metal oxide bonding at tetrahedral and octahedral sites. The influence of grain and grain boundary mechanisms on conductivity is shown by the impedance graphs. High-resistance grain boundaries become more active at low frequencies, preventing electrons from hopping between the Fe^{3+} and Fe^{2+} cations. The result is a decrease in AC conductivity. Utilising the VSM, the substance's magnetic properties were investigated. At low temperatures (3K) compared to 300K, the saturation magnetization is higher. Due to a rise in saturation magnetization over 300K, thermal fluctuations and surface spin order at the particle's surface have decreased. At 359 K Tb, the FC and ZFC modes split apart, confirming the particles' super paramagnetic nature.

Acknowledgement

The authors are thankful to SVS, Head, and BOS, Department of Physics, Osmania University, for their support.

References

[1]. G. Naveena, D. Ravinder, T.A. Babu, B. Ravinder Reddy, Sumalatha Edapalli, K. Vani, Rajender Thota, N.V.K. Prasad, Low Temperature magnetic properties of erbium doped bismuth nano-ferrites, J Mater Sci: Mater Electron. 32 (2021) 18224-18230.

[2]. P. Sivae Kistan. A. Mohan, S. Mahalakshmi, S. Jayanthi, A. Ramya, A. Janaki d, Karthik, Sol-Gel technique, characterization and photocatalytic degradation activity of Manganese doped ZnO nanoparticles, Main Group Chemistry. 22 (4) (2023) 1-4

[3]. A. H. El Foulani, A. Aamouche, F. Mohseni, J. S. Amaral, D. M. Tobaldi, R. C. Pullar, Effect of surfactants on the optical and magnetic properties of cobalt-zinc ferrite $Co_{0.5}Zn_{0.5}Fe_2O_4$, J. Alloys Comp.774 (2019) 1250-1259.

[4]. V.K. Chakradhary, A. Ansari, M. Jaleel Akhtar, Design synthesis and testing of high coercivity cobalt doped nickel ferrite nanoparticles for magnetic applications, J. Magn. Magn. Mater.469 (2019) 674-680.

[5].Tome, L. G., & Ion, R. M, Analytical studies of ferrite nanoparticles. Journal of optoelectronics and advanced materials, 12(10) (2010) 2113-2118.

[6]. Andrade, P. L. Silva, V. A. J. Maciel, J. C. Santillan, M. M. Moreno, N. O. Valladares, L. D. L. S.& Aguiar, J. A, Preparation and characterization of cobalt ferrite nanoparticles coated with fucan and oleic acid, In LACAME. 12 (2012) 211-219

[7]. V.K. Chakradhary, A. Ansari, M. Jaleel Akhtar, Design synthesis and testing of high coercivity cobalt doped nickel ferrite nanoparticles for magnetic applications, J. Magn. Magn. Mater. 469 (2019) 674-680.

[8]. Mohd. Hashim, M. Raghasudha, Sher Singh Meena, Jyoti Shah, Sagar E. Shirsath, Shalendra Kumar, D. Ravinder, Pramod Bhatt, Alimuddin, Ravi Kumar, R.K. Kotnala, Influence of rare earth ion doping (Ce and Dy) on electrical and magnetic properties of cobalt ferrites, Journal of Magnetism and Magnetic Materials 449 (2018) 319–327

[9]. C. Murugesan and G. Chandrasekaran, Impact of Gd^{3+}-substitution on the structural, magnetic and electrical properties of cobalt ferrite nanoparticles, RSC Adv. 5 (2015) 73714-73725.

[10]. Arvind Kumar,Mahendra Kumar Gora, Sanjay Kumar, Banwari Lal Choudhary, Rishi Kumar Singhal, Satya Narain Dolia, Study of electronic structure and dielectric properties of Gd-doped cobalt nanoferrites, Journal of the Korean Physical Society 81 (2022) 894–902

[11] Erum Pervaiz and I H Gul, Influence of Rare Earth (Gd^{3+}) on Structural, Gigahertz Dielectric and Magnetic Studies of Cobalt ferrite, Journal of Physics: Conference Series 439 (2013) 012015

[12] M. Kamran, M. Anis-ur-Rehman, Influence of La^{3+} substitutions on structural, dielectric and electrical properties of spinel cobalt ferrite, Ceramics International 49 (2023) 7017–7029

[13]. L. Avazpour, H. Shokrollahi, M.R. Toroghinejad, M.A. Zandi Khajeh, Effect of rare earth substitution on magnetic and structural properties of $Co_{1-x}RE_x Fe_2O_4$ (RE: Nd, Eu) nanoparticles prepared via EDTA/EG assisted sol–gel synthesis, J.Alloys Compd. 66 (2016) 441-447

[14] A.B. Kadam, Vishwanath K. Mande, S.B. Kadam, R.H. Kadam, Sagar E. Shirsath, Rameshwar B. Borade, Influence of gadolinium (Gd^{3+}) ion substitution on structural, magnetic and electrical properties of cobalt ferrites, Journal of Alloys and Compounds. 840 (2020) 155669

[15] Anil B. Mugutkar, Shyam K. Gore, Rajaram S. Mane, Khalid M. Batoo, Syed F. Adil, Santosh S. Jadhav, Magneto-structural behaviour of Gd doped nanocrystalline Co-Zn ferrites governed by domain wall movement and spin rotations, Ceramics International. 44 (2018) 21675-21683

[16] Y. Belaiche, K. Minaoui, M. Ouadou, M. Elansary, C. Ahmani Ferdi, New nanosized (Gd^{3+}, Sm^{3+}) co-doped zinc ferrite: Structural, magnetic and first-principles studyPhysica B: Condensed Matter. 619 (2021) 413262

[17] B. Nandan, M. Bhatnagar, S.C. Kashyap, Static magnetic properties and cation distribution in partially inverse polycrystalline Ni–Co ferrites, Appl. Phys. A 124 (2018) 1–8

[18] Y.T. Prabhu, K.V. Rao, X-ray analysis by Williamson-Hall and size-strain plot methods of ZnO nanoparticles with fuel variation. World J. Nano Sci. Eng. 4 (2014) 21–28

[19] V. Kanchana, kistan andiyappan, silver-alumina impregnated maghemite/magnetite nanocomposites for effective removal of chromium(vi) from the tannery discharge, asian journal of chemistry. 35 (8) (2023) 1899-1906

[20] R.D. Waldron, Infrared Spectra of Ferrites, phys. Rev 99 (1995) 1727-1735

[21] R.S. Yadav, I. Kuřitka, J. Vilcakova, J. Havlica, L. Kalina, P. Urbánek, M. Machovsky, D. Skoda, M. Masař, M. Holek, Sonochemical Synthesis of Gd^{3+} doped CoFe2O4 Spine Ferrite Nanoparticles and Its Physical Properties, Ultrasonics Sonochemistry. 40 (2017) 773-783.

[22] P. Samoila, C. Cojocaru, L. Sacarescu, P. P. Dorneanu, A.-A. Domocos, Aurelian Rotaruca., Remarkable catalytic properties of rare-earth doped nickel ferritessynthesized by sol-gel autocombustion with maleic acid as fuel for CWPO of dyes, Applied Catalysis B: Environmental. 202 (2017) 21–32.

[23] C Esther Jeyanthi, C Karnan, A Kistan, R Siddheswaran, Impact of cobalt doping on magnetic and structural properties in Ce1− xCoxO2 (x= 0.1, 0.2 and 0.3) ceramics synthesized by combustion method, Inorganic Chemistry Communications. 153 (2023) 110836.

[24] C.H. Lui, Z. Li, K.F. Mak, E. Cappelluti, T.F. Heinz, Observation of an electrically tunable band gap in trilayer graphene, Nat. Phys. 7 (2011) 944–947

[25]. Y. Lu, M. Yousaf, M.N. Akhtar, A. Noor, M. Akbar, M.A.K.Y. Shah, S. Yan, F. Wang, Effect of Gd and Co contents on the microstructural, magneto-optical and electrical characteristics of cobalt ferrite ($CoFe_2O_4$) nanoparticles Ceram. Int., 48 (2022) 2782-2792

[26] W.R. Agami, Effect of neodymium substitution on the electric and dielectric properties of Mn-Ni-Zn ferrite,Physica B: Condensed Matter 534 (2018) 17-21

[27] Javed, F. Iqbal, P.O. Agboola, M.A. Khan, M.F. Warsi, I. Shakir, Structural, electrical and magnetic parameters evaluation of nano-crystalline rare earth Nd^{3+} - substituted nickel-zinc spinel ferrite particles, Ceram. Int. 45 (2019) 11125–11130.

[28].C. G. Koops. (1951) On the dispersion of resistivity and dielectric constant of some semiconductors at audio frequencies Phys. Rev., 83, 121.

[29].R.C. Kambale, P.A. Shaikh, C.H. Bhosale, K.Y. Rajpure, Y.D. Kolekar, Dielectric properties and complex impedance spectroscopy studies of mixed Ni–Co ferrites, Smart Mater. Struct., 18 (2009) 085014.

[30]. B. Debnath, S. Parvin, H. Dixit, S. Bhattacharyya, Oxygen-Defect-Rich Cobalt Ferrite Nanoparticles for Practical Water Electrolysis with High Activity and Durability, Chemsuschem. 15 (2020) 3875–3886 .

[31].F.R. Mariosi, J. Venturini, A.C. Viegas, C.P. Bergmann, Influence of Co^{4+}-Ca^{2+} substitution on Structural, Microstructure, Magnetic, Electrical and Impedance Characteristics of M- type Barium-Strontium Hexagonal ferrites, Ceram. Int. 46(3) (2020) 2772–2779.

[32].M.D. Harun-Or-Rashid, M. Nazrul Islam, M. Arifuzzaman, A.K.M. Akther Hossain, Effect of sintering temperature on the structural, morphological, electrical, and magnetic properties of Ni Cu Zn and Ni Cu Zn Sc ferrites, J Mater Sci: Mater Electron. 32 (2021) 2505-2523.

[33].M. N. Akhtar, M. Yousaf, Lu. Yuzheng, M. A. Khan, Ali Sarosh, Mina Arshad, Misbah Niamat, Muhammad Farhan, A. Ahmad, M. U. Khallidoon, Physical, structural, conductive and magneto-optical properties of rare earths (Yb, Gd) doped Ni-Zn spinel nano ferrites for data and energy storage devices, Ceram. Int. 47 (2021) 11878-11886.

[34]. M.Kamran, M.Anis-ur-Rehman, Enhanced transport properties in Ce doped cobalt ferrites nanoparticles for resistive RAM applications, Journal of Alloys and Compounds. 822 (2020) 153583

[35].Vijaya Anandan Veerasamy Alagarsamy, Kistan Andiyappan, Saral Abdul Kadar Avuliya, Thaminum Ansari Abubacker, Retarding of preliminary chemical pollutants from dye effluent by metal nano particles synthesized using flower extract of catharanthus roseus, Oriental Journal of Chemistry. 34(1) (2018) 381

[36].C. Esther Jeyanthi and K. Uma 18) Kistan, A, V. Kanchana, Antimicrobial, antifungal, larvicidal, and antioxidant activity of freshly prepared cyanopyridine derivatives,Rasayan Journal of Chemistry, Rasayan Journal of Chemistry, 16(4) (2023) 2171-2180

[37]. V Ludhiya, N. Hari kumar, D Ravinder, Avula Edukondalu, Structural, optical, dielectric and magnetic properties of Nd^{3+} ion substituted Ni-Mg-Cu spinel ferrites. Inorg Chem Commun. 150 (2023) 110558.

[38]. N. Hari kumar, D. Ravinder, A. Edukondalu, Synthesis, structural, antimicrobial activity and dielectric properties of Ce^{3+}-doped Ni–Zn nano-ferrites, Appl. Phys. A 128 (2022) 978.

[39]. Banoth Baburao, N. Hari kumar, Avula Edukondalu, M. Venkata Narayana, D. Ravinder, optical, DC electrical, thermo-electric, dielectric and magnetic properties of $Mg_{0.8}Zn_{0.2}Gd_xFe_{2-x}O_4$ nanoparticles synthesised by citrate-gel auto combustion method. Inorg. Chem. Commun. 148 (2023) 110355.

Figures

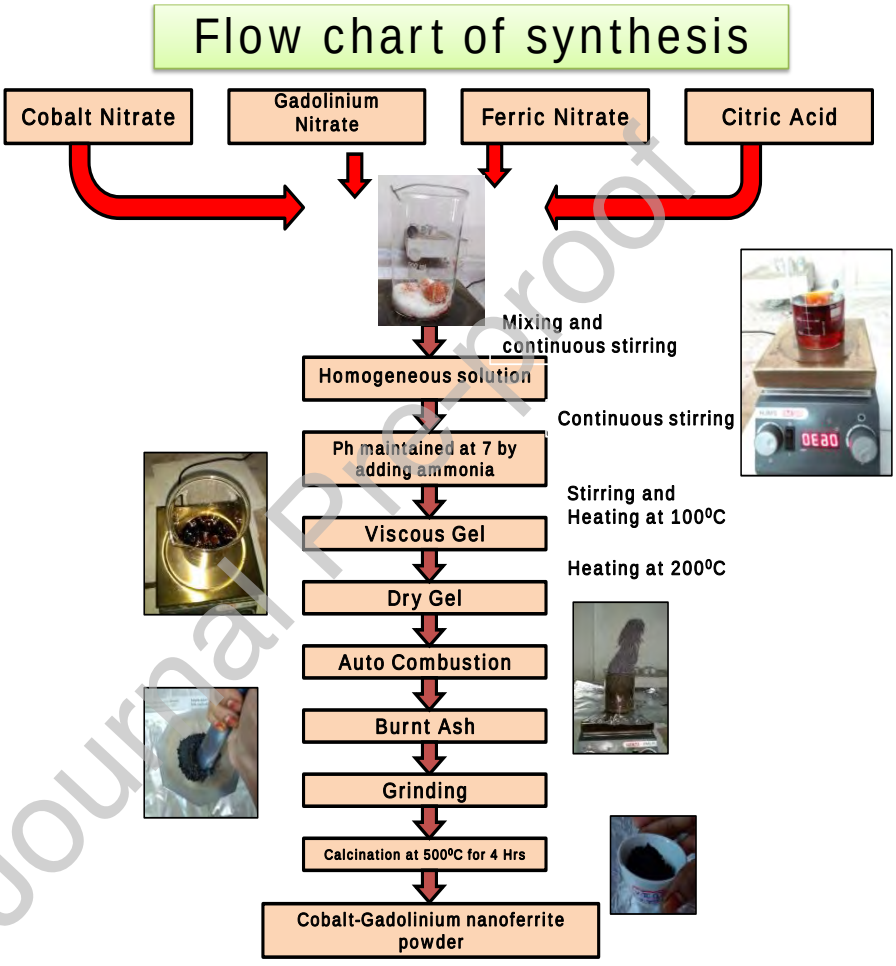

Fig.1. *Flow chart of* $CoGd_xFe_{2-x}O_4$ *nanoferrites*.

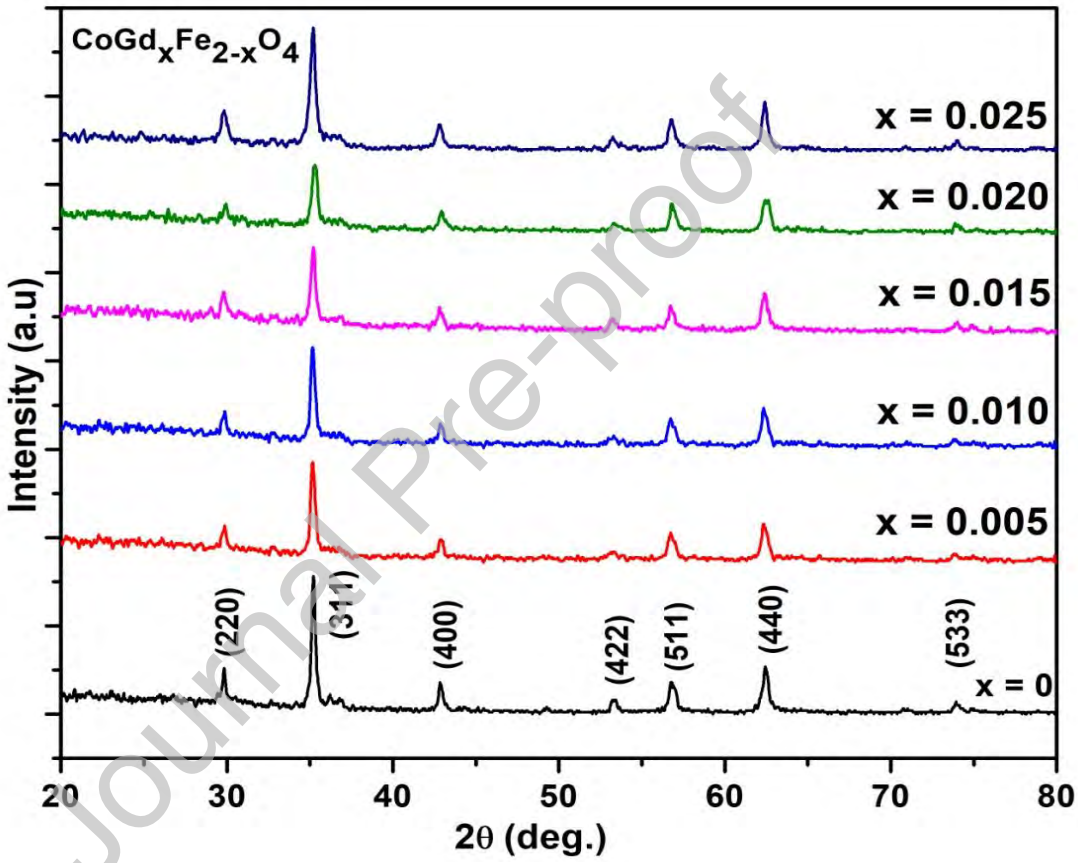

Fig. 2. *XRD plots of $CoGd_xFe_{2-x}O_4$ (x= 0-0.025 in an interval of 0.005) nanoferrites*

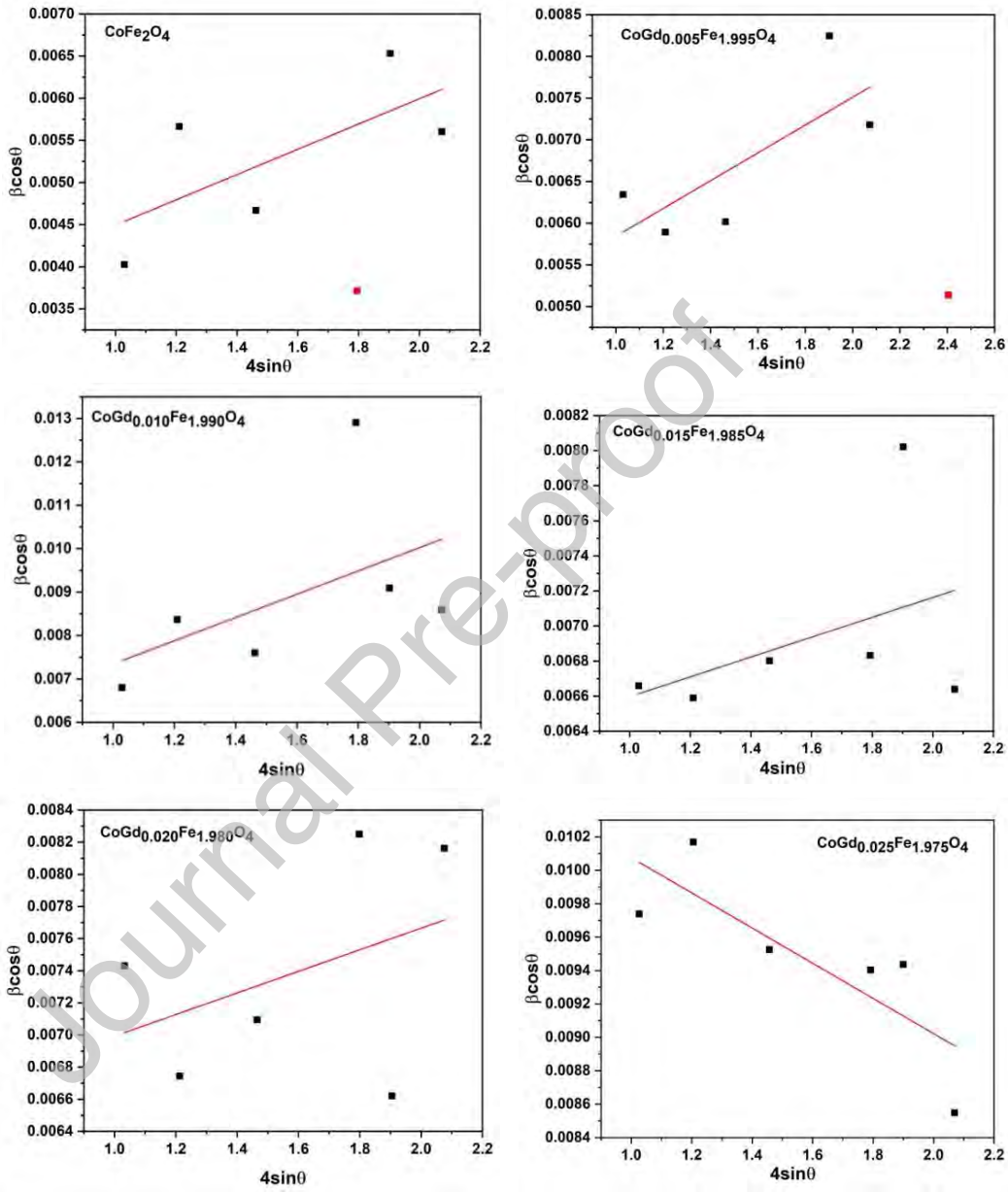

Fig. 3. *W-H plots of $CoGd_xFe_{2-x}O_4$ (x= 0-0.025 in an interval of 0.005) nanoferrites.*

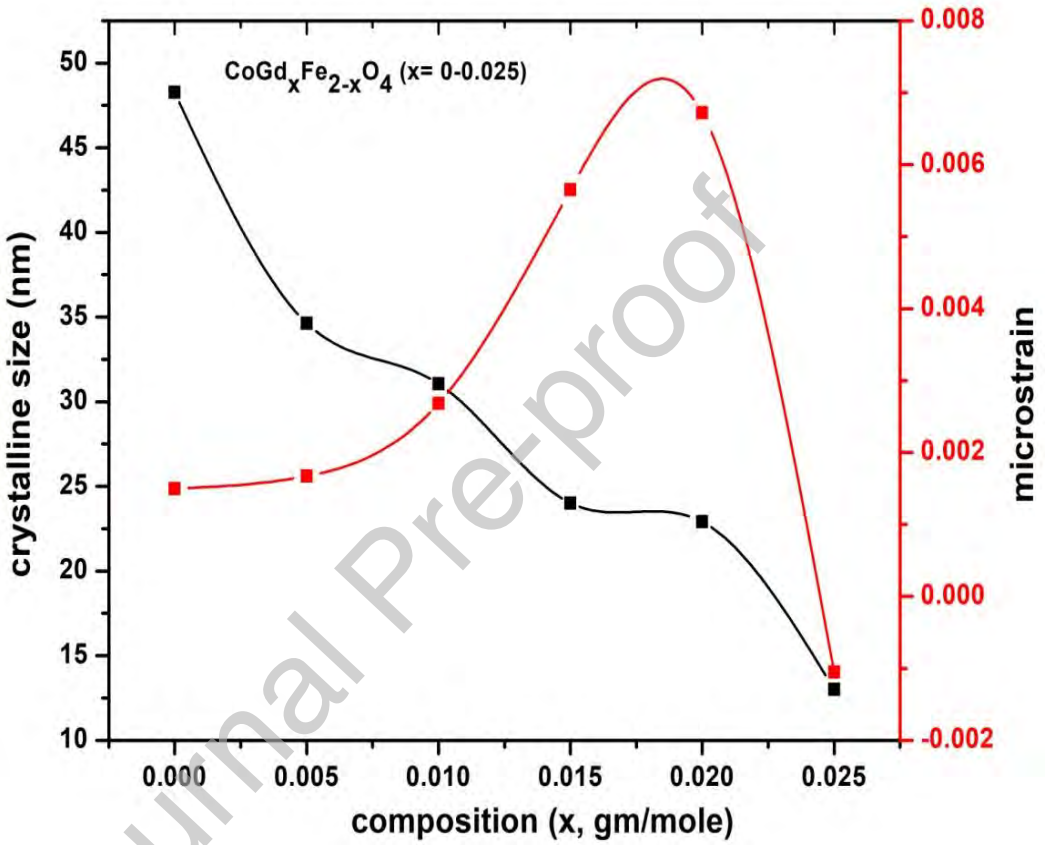

Fig. 4.*variation of crystalline size and micro strain with respect to composition of* $CoGd_xFe_{2-x}O_4$ *(x= 0-0.025 in an interval of 0.005) ferrites*

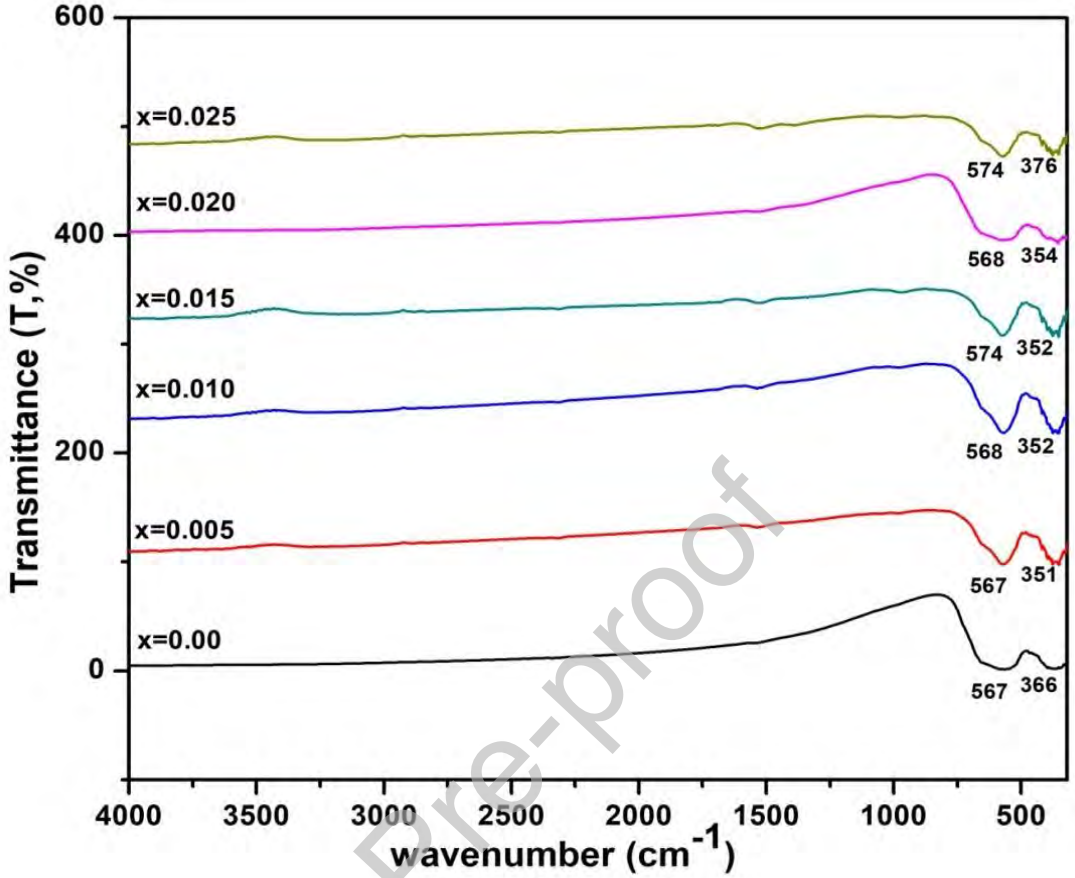

Fig. 5. *FTIR spectra of $CoGd_xFe_{2-x}O_4$ (x= 0-0.025 in an interval of 0.005) nanoferrites*

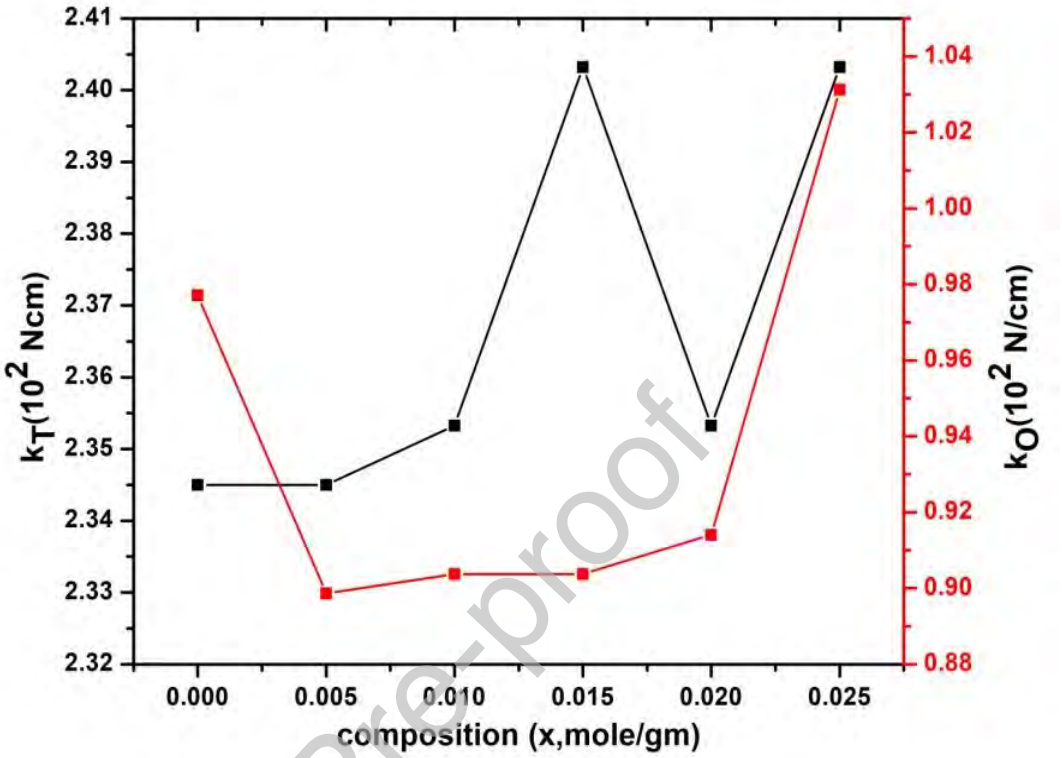

Fig. 6. *variation of force constants with composition of* $CoGd_xFe_{2-x}O_4$ *(x= 0-0.025 in an interval of 0.005) nanoferrites*

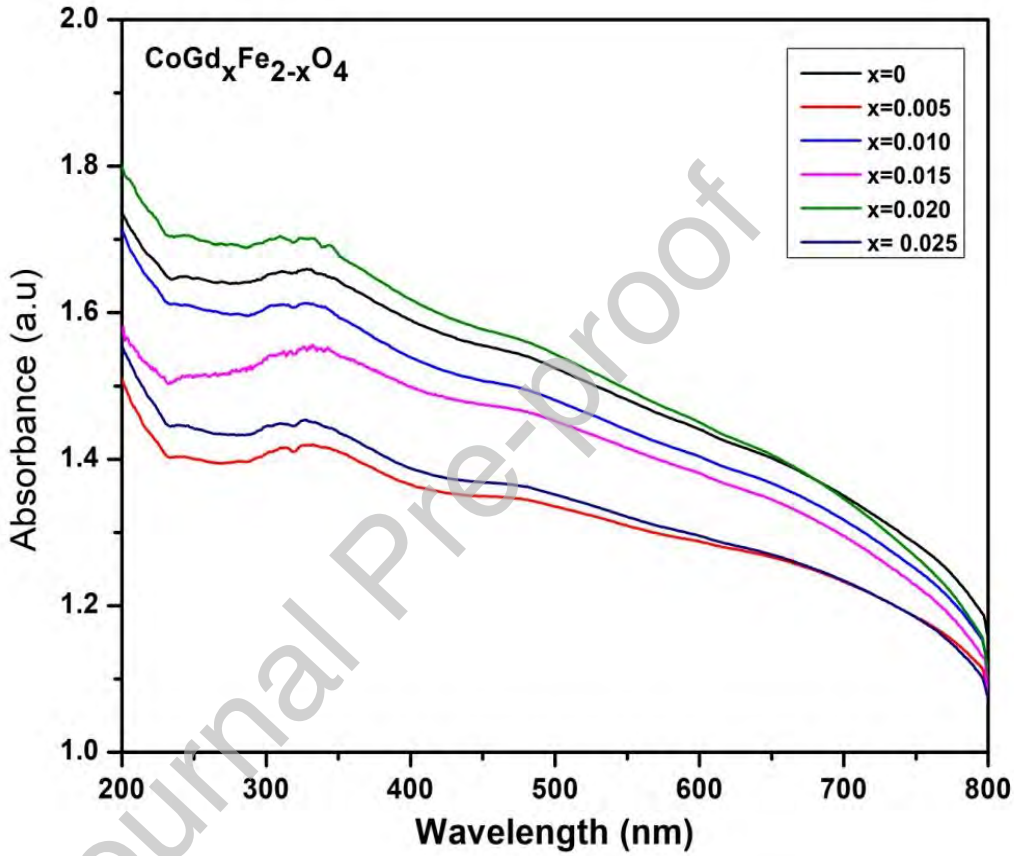

Fig. 7. *UV-Visible absorption spectra of $CoGd_xFe_{2-x}O_4$ (x= 0-0.025 in an interval of 0.005) nanoferrites.*

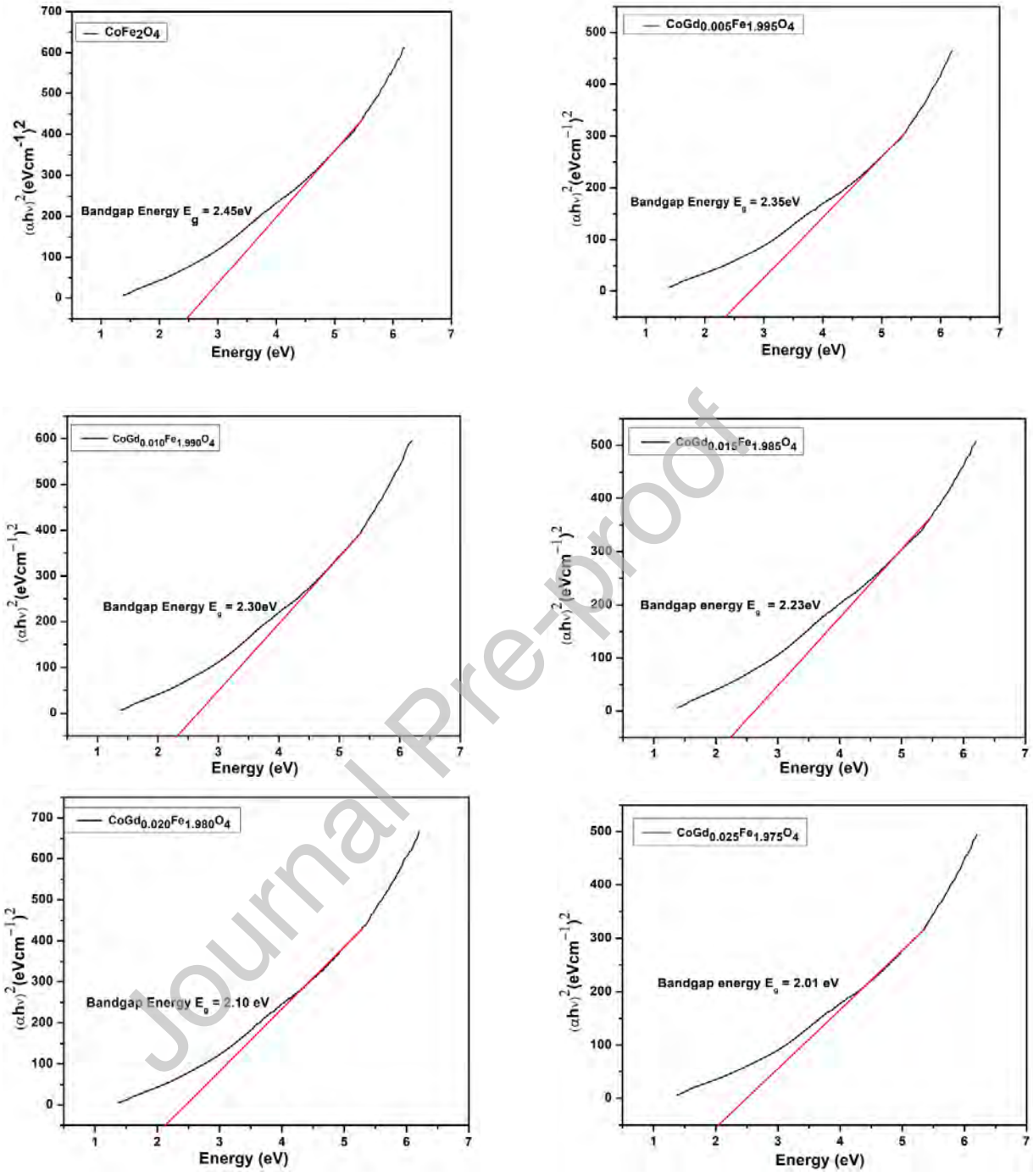

Fig. 8. *Optical bandgap analysis of $CoGd_xFe_{2-x}O_4$ (x= 0-0.025 in an interval of 0.005) nanoferrites.*

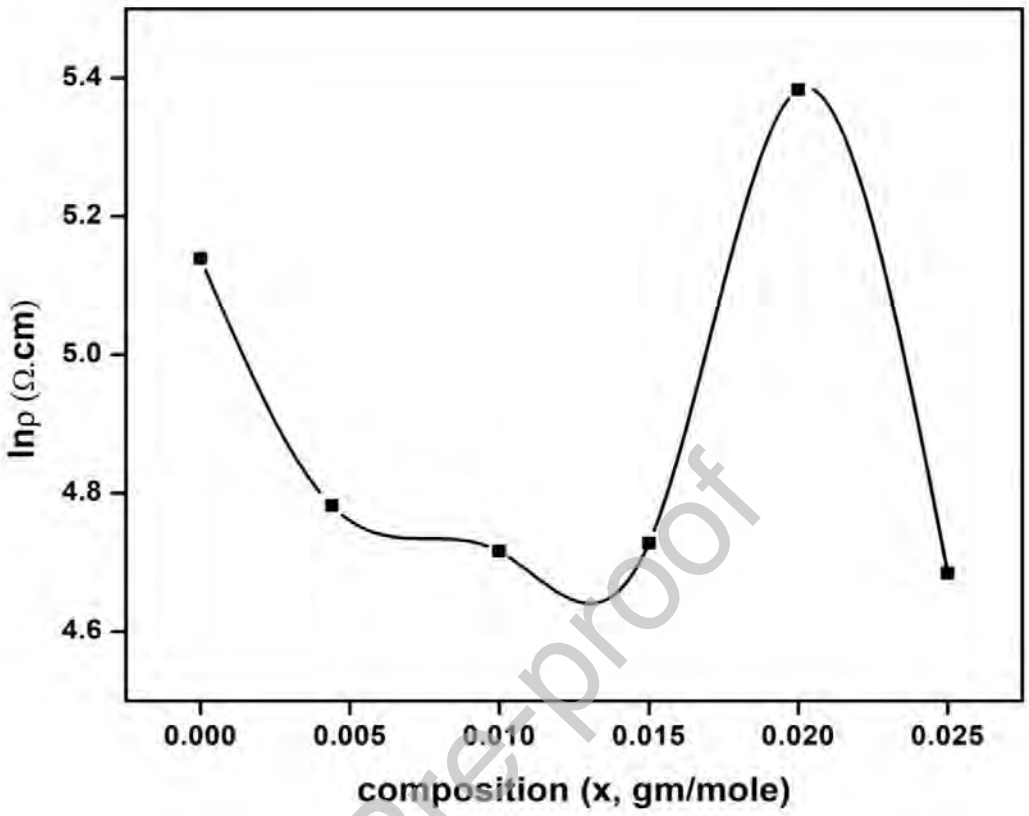

Fig. 9. *Variation of DC electrical resistivity (lnρ) with composition x for* $CoGd_xFe_{2-x}O_4$ *(x= 0.0- 0.025) samples.*

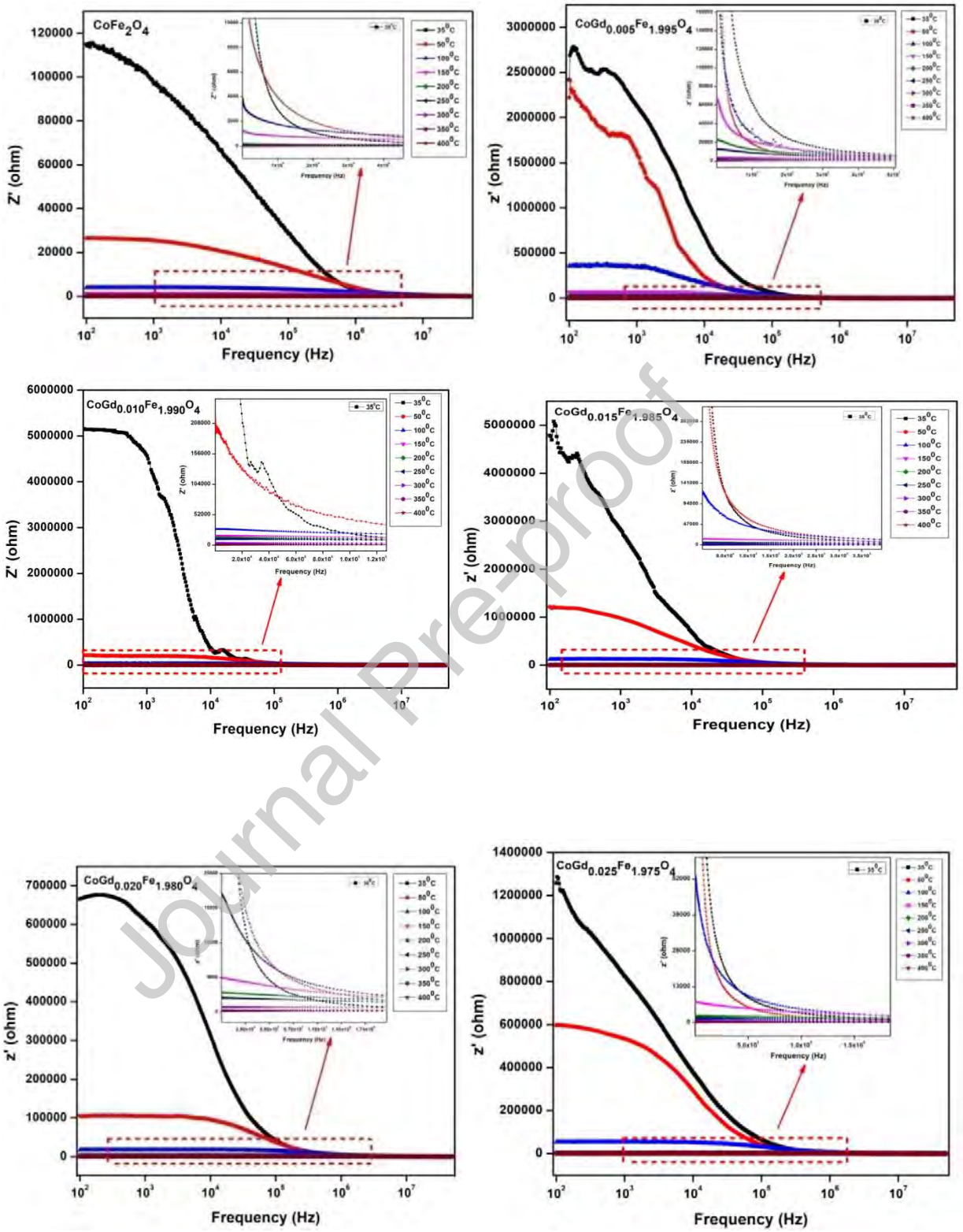

Fig. 10(a-f).*Variation of real part of impedance (Z') as a function of frequency of $CoGd_xFe_{2-x}O_4$ (x= 0-0.025 in an interval of 0.005) nanoferrites.*

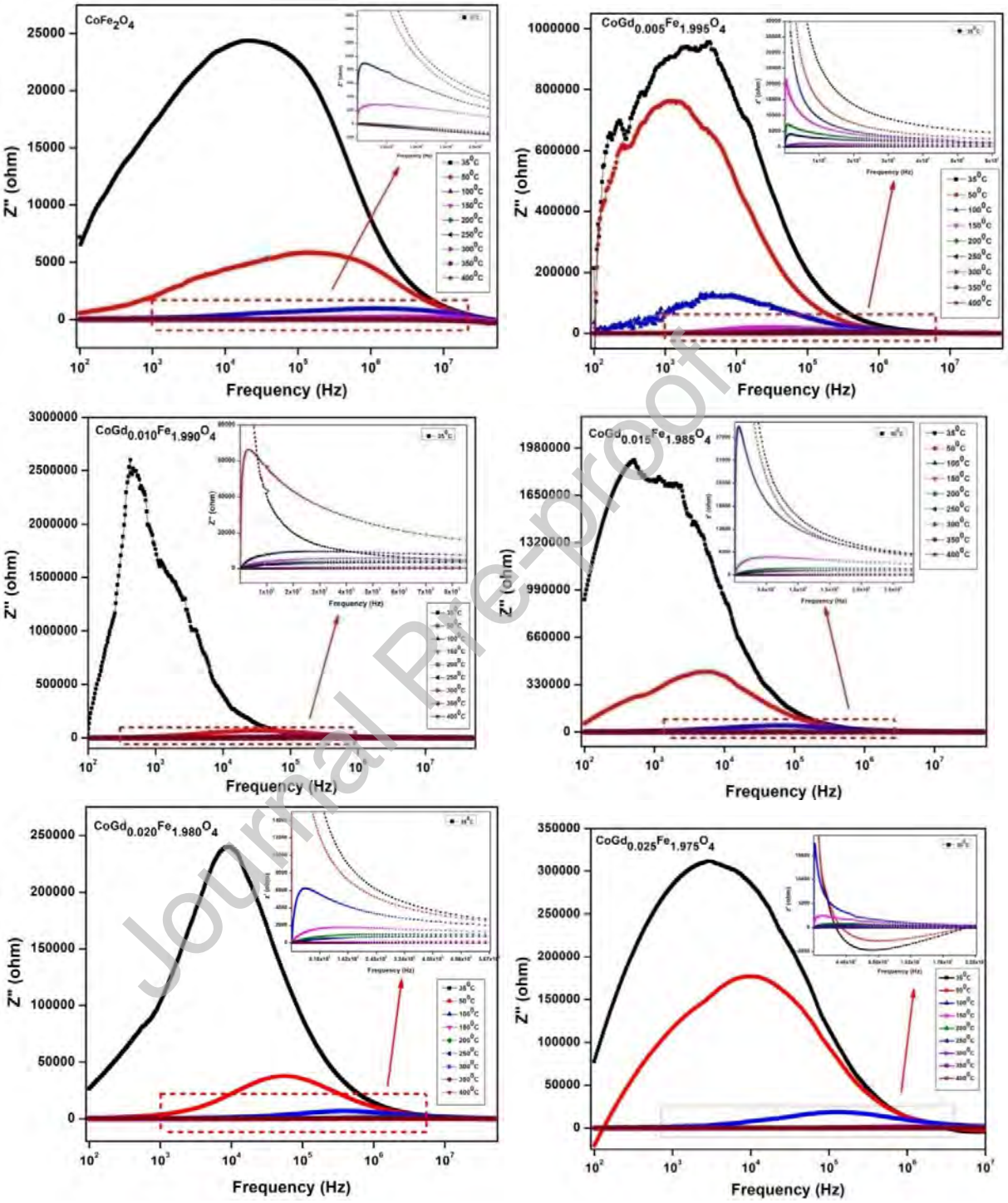

Fig. 11(a-f). *Variation of imaginary part of impedance (Z″) as a function of frequency of* $CoGd_xFe_{2-x}O_4$ *(x= 0-0.025 in an interval of 0.005) nanoferrites.*

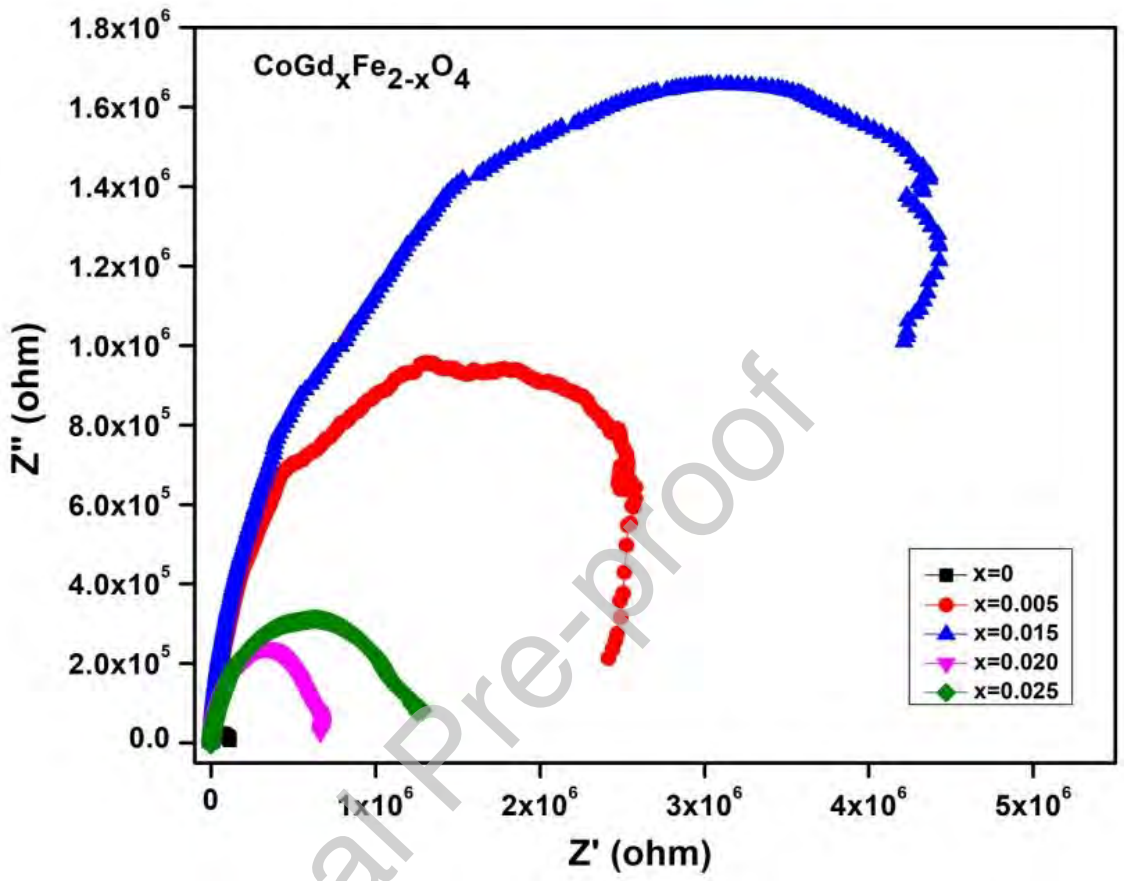

Fig. 12. *Complex impedance spectra/Nyquist plots (Z' Vs –Z'') of $CoGd_xFe_{2-x}O_4$ (x= 0-0.025 in an interval of 0.005) ferrite at room temperature.*

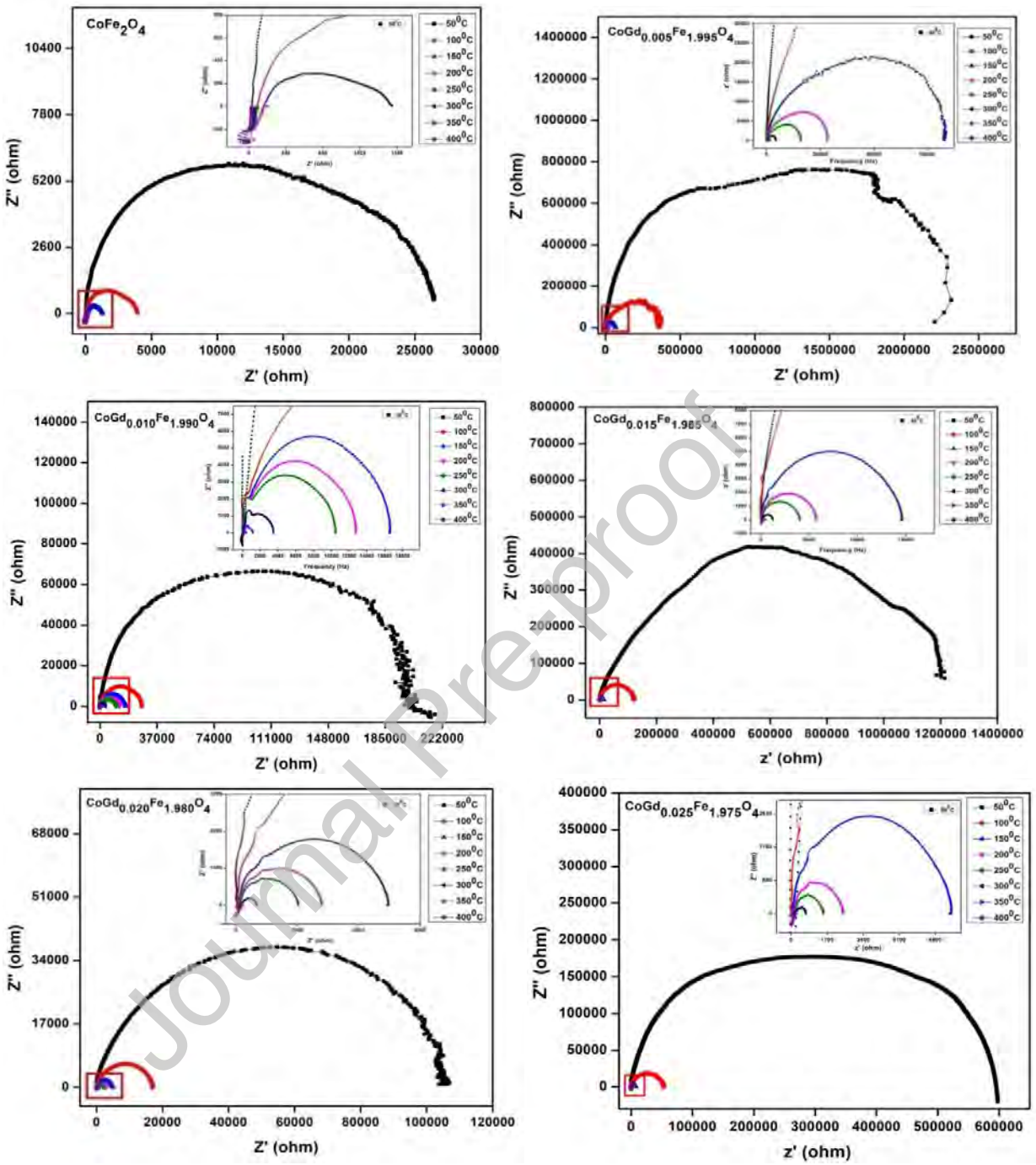

Fig. 13(a-f). *Complex impedance spectra/Nyquist plots (Z' Vs –Z'') of $CoGd_xFe_{2-x}O_4$ (x= 0-0.025 in an interval of 0.005) ferrite at selected temperatures.*

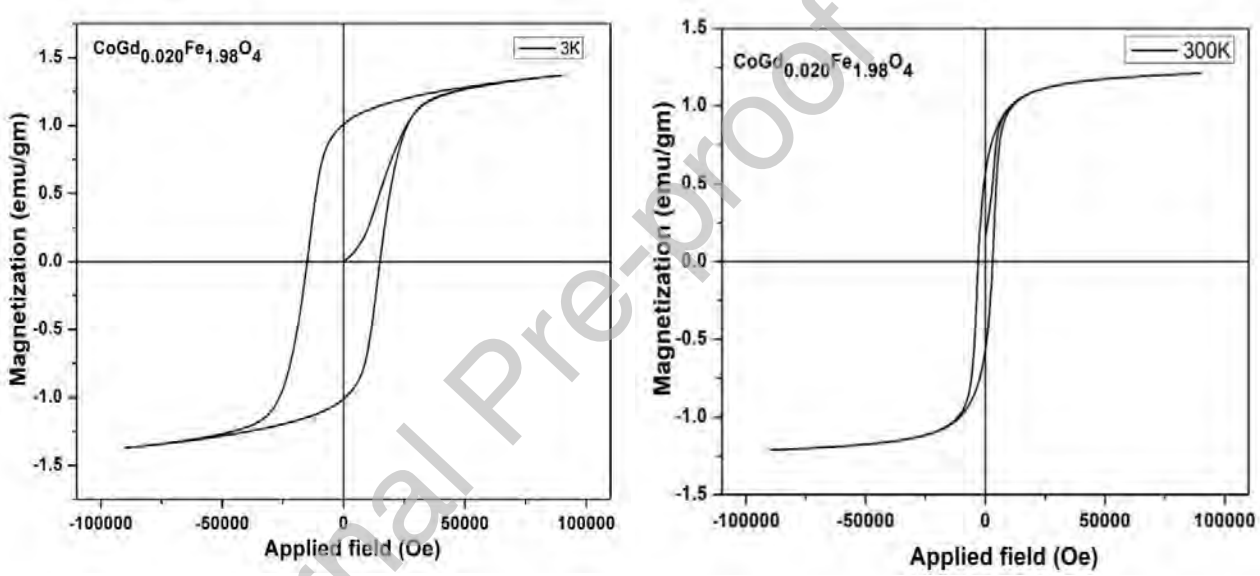

Fig. 14(a,b).*Variation of magnetization with applied field of $CoGd_xFe_{2-x}O_4$ (x=0.020) sample.*

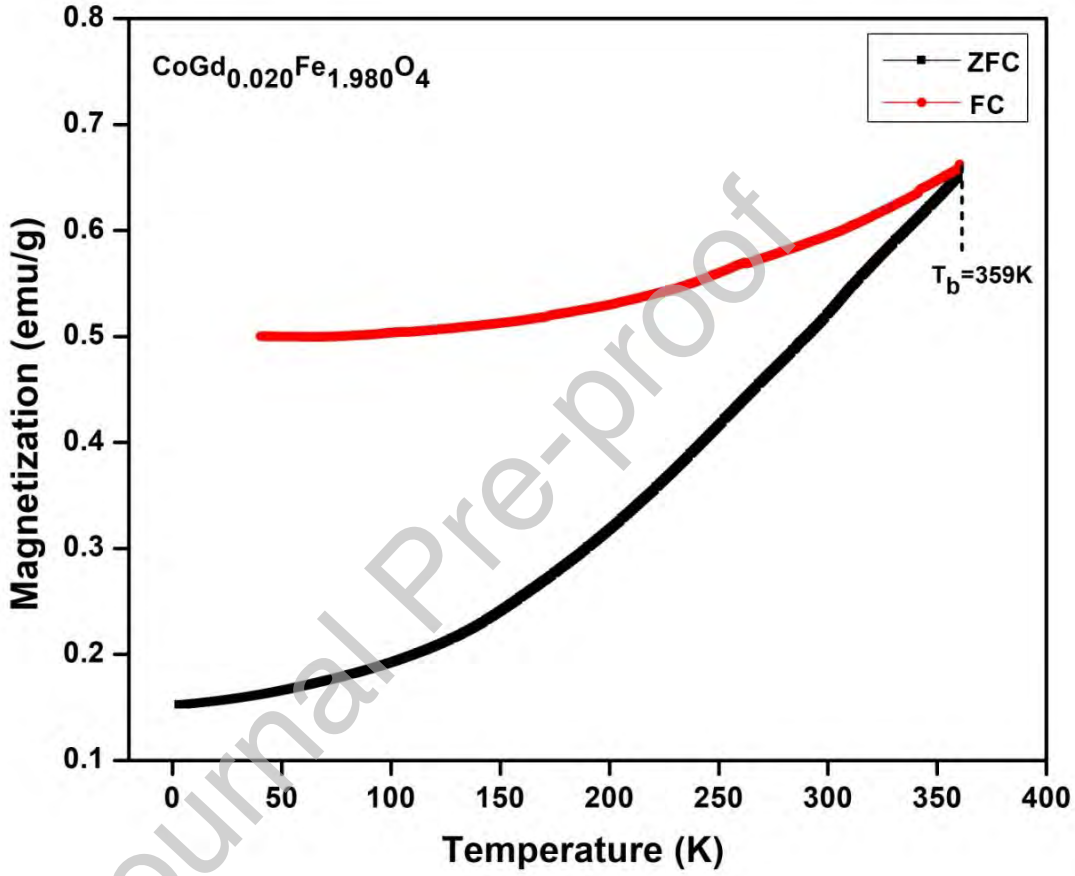

Fig. 15.*Variation of magnetization with temperature curve recorded in FC and ZFC modes for* $CoGd_xFe_{2-x}O_4$ *(x=0.020) sample in an external magnetic field of 100Oe.*

Table 1. *Crystallite size, lattice constant, volume, X-ray density, hopping lengths(L_A & L_B) and strain for $CoGd_xFe_{2-x}O_4$ (x=0-0.025 in an interval of 0.005) nanoferrites*

Samples	**Average crystallite size, D(nm)**	**Lattice constant, a(Å)**	**Volume of unit cell, V a=b=c ($Å^3$)**	**X-ray density, d_x(gm/cm^3)**	**Hopping length for site A, L_A (Å)**	**Hopping length for site B, L_B (Å)**	**Strain (ε)**
$CoFe_2O_4$	48.27	8.45	603.9	5.160	3.6601	2.9885	0.0015
$CoGd_{0.005}Fe_{1.995}O_4$	34.64	8.45	605.3	5.159	3.6630	2.9908	0.00167
$CoGd_{0.010}Fe_{1.990}O_4$	31.07	8.46	605.5	5.169	3.6633	2.9911	0.00268
$CoGd_{0.015}Fe_{1.985}O_4$	24.01	8.45	604.9	5.185	3.6621	2.9901	0.00565
$CoGd_{0.020}Fe_{1.980}O_4$	22.91	8.42	599.0	5.247	3.6502	2.9804	0.00672
$CoGd_{0.025}Fe_{1.975}O_4$	13.01	8.45	605.2	5.205	3.6628	2.9906	-0.00105

Table 2. *FTIR modes (v_1, v_2) and force constant (k_T and k_o) for $CoGd_xFe_{2-x}O_4$ (x= 0-0.025 in an interval of 0.005) nanoferrites.*

Composition (x)	**v_1(cm^{-1})**	**v_2(cm^{-1})**	**$k_T x10^2$ (N/m)**	**$k_O x10^2$ (N/m)**
0.00	567	366	2.34	0.97
0.005	567	351	2.34	0.89
0.010	568	352	2.35	0.90
0.015	574	352	2.40	0.90
0.020	568	354	2.35	0.91
0.025	574	376	2.40	1.03

Table 3. *saturation magnetization (M_s), coercivity (H_c), remanance magnetization (M_r), remanance ratio (M_r/M_s), anisotropy constant (K) and magnetic moment (B_M) values of $CoGd_{0.020}Fe_{1.98}O_4$ sample at 3K and 300K* **.**

Sample	**Measured at Temperature (K)**	**Saturation magnetization M_S(emu/g)**	**Coercivity H_c (Oe*10^4)**	**Remanent magnetization M_r (emu/g)**	**Remanance ratio= M_r/M_s**	**Anisotropy constant (K) erg/Oe**	**Magnetic moment (B_M)**
$CoGd_{0.020}Fe_{1.980}O_4$	**3**	73.28	1.5	53.86	0.7349	114.5	3.1049
	300	64.75	0.9	32.66	0.5044	60.703	2.7434

Graphical Abstract

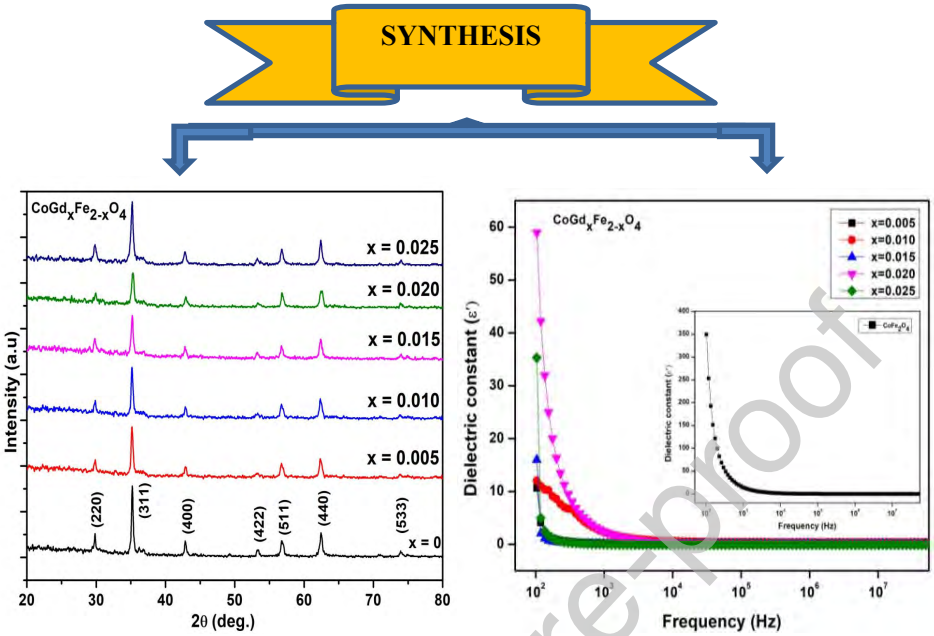

Declaration of Conflict of Interest

The authors declare that they have no known competing financial interests or personal relationships that could have appeared to influence the work reported in this paper.